Redox control on nitrogen isotope fractionation during planetary core formation

Célia Dalou, Evelyn Füri, Cécile Deligny, Laurette Piani, Marie-Camille Caumon, Mickaël Laumonier, Julien Boulliung, Mattias Edén

Redox control on nitrogen isotope fractionation during planetary core formation

Celia Dalou[a,1], Evelyn Füri[a], Cécile Deligny[a], Laurette Piani[a], Marie-Camille Caumon[b], Mickael Laumonier[c], Julien Boulliung[a], and Mattias Edén[d]

[a]Centre de Recherches Pétrographiques et Géochimiques, UMR 7358, CNRS–Université de Lorraine, 54501 Vandoeuvre-lès-Nancy Cedex, France; [b]GeoRessources, Université de Lorraine, CNRS, 54506 Vandœuvre-lès-Nancy, France; [c]Université Clermont Auvergne, CNRS, Institut de Recherche pour le Développement, Observatoire Physique du Globe de Clermont-Ferrand, Laboratoire Magmas et Volcans, F-63000 Clermont-Ferrand, France; and [d]Physical Chemistry Division, Department of Materials and Environmental Chemistry, Arrhenius Laboratory, Stockholm University, SE-106 91 Stockholm, Sweden

Edited by Mark H. Thiemens, University of California San Diego, La Jolla, CA, and approved June 6, 2019 (received for review December 26, 2018)

The present-day nitrogen isotopic compositions of Earth's surficial (^{15}N-enriched) and deep reservoirs (^{15}N-depleted) differ significantly. This distribution can neither be explained by modern mantle degassing nor recycling via subduction zones. As the effect of planetary differentiation on the behavior of N isotopes is poorly understood, we experimentally determined N-isotopic fractionations during metal–silicate partitioning (analogous to planetary core formation) over a large range of oxygen fugacities (ΔIW $-3.1 < \log fO_2 <$ ΔIW -0.5, where ΔIW is the logarithmic difference between experimental oxygen fugacity [fO_2] conditions and that imposed by the coexistence of iron and wüstite) at 1 GPa and 1,400 °C. We developed an in situ analytical method to measure the N-elemental and -isotopic compositions of experimental run products composed of Fe–C–N metal alloys and basaltic melts. Our results show substantial N-isotopic fractionations between metal alloys and silicate glasses, i.e., from -257 ± 22‰ to -49 ± 1‰ over 3 log units of fO_2. These large fractionations under reduced conditions can be explained by the large difference between N bonding in metal alloys (Fe–N) and in silicate glasses (as molecular N_2 and NH complexes). We show that the δ^{15}N value of the silicate mantle could have increased by ∼20‰ during core formation due to N segregation into the core.

nitrogen isotopes | fractionation | core formation | speciation | ion probe

The bulk silicate Earth is the largest nitrogen reservoir on Earth, containing 3 to 11 times more N ($27 \pm 16 \times 10^{18}$ kg N) than the present-day atmosphere (4×10^{18} kg N or the present atmospheric nitrogen abundance [PAN]) (1). In particular, Earth's mantle is estimated to contain 6 PAN (up to 24×10^{18} kg N) (1), which is 12 times more than the continental crust (0.5 PAN) (1). The 2 stable isotopes of nitrogen, ^{14}N and ^{15}N (∼99.6% and ∼0.4% of present atmospheric N_2, respectively), are used to trace fluxes between surface and deep-Earth reservoirs. N stable isotopic compositions are conventionally normalized to the present atmospheric value and reported as follows:

$$\delta^{15}\mathrm{N}[‰] = 1{,}000 \cdot \left[\left(\frac{^{15}\mathrm{N}/^{14}\mathrm{N}_{\mathrm{sample}}}{^{15}\mathrm{N}/^{14}\mathrm{N}_{\mathrm{atm}\mathrm{N}_2}}\right) - 1\right]. \quad [1]$$

The current N-isotopic distribution among terrestrial reservoirs shows an unexplained difference (2) between the ^{15}N-depleted mantle [δ^{15}N = -5 ± 2‰ in diamonds and midocean ridge basalts (MORBs) (3)] and the ^{15}N-enriched surface [δ^{15}N = +6‰ in sediments, and 0‰ (by definition) in the present-day atmosphere (4)]. Contradictory to these observations, diffusion-controlled N_2 degassing (5) of the mantle is expected to preferentially segregate ^{14}N into the atmosphere (Graham's law), which would enrich the mantle in ^{15}N. Equilibrium degassing of MORBs modeled by Rayleigh distillation (5, 6) enriches the residual melt in ^{15}N, but this fractionation is limited to 1 to 1.5‰ (7). Recycling (subduction) of surficial material is expected to increase the δ^{15}N value of the mantle because sediments and altered continental crust are enriched in ^{15}N (3) by biological processes [i.e., N fixation pathways and N cycling within microbial communities (e.g., refs. 8 and 9)] and metamorphism-related devolatilization of N (4), respectively. Marty and Dauphas (7) proposed that the mantle's N-isotopic signature corresponds to that of recycled Archean sediments; this hypothesis has been actively debated (10) because the δ^{15}N values of ancient sediments are highly variable [−6.2 to +13‰ (8)]. Hence, neither degassing processes nor recycling can explain the mantle's N-isotopic signature relative to the atmosphere (3).

An alternative explanation of the mantle's N-isotopic signature is the heterogeneous accretion of the Earth from materials with δ^{15}N values as low as −40‰ (11), the lowest value measured on Earth in deep diamonds (12). Indeed, the low δ^{15}N values of enstatite chondrites [−45 to −15‰ (13)] compared with carbonaceous chondrites [+15 to +55‰ (14)] suggest an enstatite chondrite origin of Earth's nitrogen (11, 12). After accretion, planetary differentiation processes could have modified the initial N budget and isotopic signature of the mantle. Core–mantle differentiation, magma ocean solidification/crystallization, and magma ocean degassing are key stages of early planetary evolution. These 3 processes could potentially result in N-isotopic

Significance

The origin and evolution of Earth's nitrogen is often discussed by comparing the large variation of N-isotopic compositions among Earth's building blocks (chondrites) to the signatures of various terrestrial reservoirs. Here, we demonstrate that planetary differentiation processes, such as core formation, may have significantly modified the N-isotopic composition of the proto-Earth. During core–mantle differentiation, a significant amount of isotopically light N entered Earth's core, producing an isotopic fractionation much larger than has been observed for other geochemical tracers of core formation. The magnitude of N-isotopic fractionation varies significantly as a function of the redox history of the early Earth. Therefore, distinct N-isotopic ratios among Earth's reservoirs or between planetary bodies may reflect different planetary evolution processes as opposed to different N sources.

Author contributions: C. Dalou designed research; C. Dalou and M.L. performed research; E.F. and M.E. contributed new reagents/analytic tools; C. Dalou, E.F., C. Deligny, L.P., M.-C.C., and J.B. analyzed data; and C. Dalou wrote the paper with input from all authors.

The authors declare no conflict of interest.

This article is a PNAS Direct Submission.

[1]To whom correspondence may be addressed. Email: cdalou@crpg.cnrs-nancy.fr.

This article contains supporting information online at www.pnas.org/lookup/suppl/doi:10.1073/pnas.1820719116/-/DCSupplemental.

Published online July 1, 2019.

fractionations sufficient to explain the large differences in current $\delta^{15}N$ values among the distinct terrestrial reservoirs (3).

Recent studies have revealed that a significant fraction of N could have been segregated into the core during the late stages of core formation (15–22). Investigation of the effect of core formation on the evolution of the bulk mantle $\delta^{15}N$ value requires knowledge of the N-isotopic fractionation factors between metal and silicate phases. Li et al. (16) measured the $^{15}N/^{14}N$ fractionation between metal and basaltic glasses ($\Delta^{15}N^{metal\text{-}silicate} = \delta^{15}N^{metal} - \delta^{15}N^{silicate}$) at 1.5 to 7 GPa and 1,600 to 1,800 °C. They showed that during metal–silicate segregation, the silicate melt is enriched in ^{15}N by 3.5 ± 2.5‰ relative to the coexisting liquid Fe–C–N metal alloy. These experimental results are consistent with an equilibrium isotopic fractionation, which causes the lighter isotope to be enriched in the most reduced phase (23). However, the large uncertainties on their isotopic fractionation factors (typically 2.5‰) preclude any definitive conclusion on the effect of metal–silicate N segregation. Additionally, the relatively narrow range of oxygen fugacities (fO_2, reported as the logarithmic difference between experimental fO_2 conditions and the iron–wüstite buffer [IW]) explored by Li et al. [ΔIW −0.11 to −0.35 (16)] presumably corresponds only to the latest stage of core–mantle differentiation (24). Although the fO_2 conditions of Earth's core formation are still debated (e.g., refs. 25–27), recent models acknowledge that the Earth accreted from highly reduced materials (typically around ΔIW −5) and that its fO_2 increased throughout the late stages of accretion and core–mantle differentiation (reaching ΔIW −2 to IW during the late stages of the magma ocean; refs. 24, 26, and 28). Recent studies have shown fO_2 to be the main control on N partitioning during metal–silicate segregation (17–22) because it determines the N speciation in the silicate phase (17, 29). N speciation, in turn, is expected to dictate $\Delta^{15}N^{metal\text{-}silicate}$ (29). The magnitude of isotopic fractionations is proportional to the difference in bond stiffness and vibration modes between equilibrated phases (30, 31), i.e., $\Delta^{15}N^{metal\text{-}silicate}$ is determined by the bonding of N in the metal (as Fe–N) and silicate melt [as N–N vs. N–H complexes depending on fO_2 conditions (29)]. Therefore, fO_2 is expected to play a fundamental role in the evolution of the $\delta^{15}N$ value of Earth's mantle, and thus in the establishment of the observed difference between surficial and deep N-isotopic signatures.

In this study, we investigated the redox effect on N-isotopic fractionation during metal–silicate N partitioning in samples quenched at 1 GPa and 1,400 °C in a piston-cylinder (Laboratoire Magmas et Volcans, Clermont-Ferrand, France). We explored fO_2 conditions ranging from Fe–FeO equilibrium (IW) to ΔIW −3 (i.e., 3 orders of magnitude more reducing), consistent with the inferred conditions of core formation (32). The duration of the experiments was 6 h, which is sufficient to reach compositional equilibrium (17). The starting material compositions comprised a Fe-rich haplo-basalt [similar to the Humphrey basalt composition of Dalou et al. (17) and Armstrong et al. (33)] to promote the segregation of large metal blobs under reducing conditions, and a haplo-andesite composition similar to that used by Zhang et al. (34). These mafic to intermediate compositions were chosen as analogs of planetary magma ocean compositions (35). The fO_2 of the samples was changed (not controlled) by adding 0.5 to 4 wt% Si_3N_4 [a reducing agent (17)] to the starting compositions. To "spike" the samples in ^{15}N, we used mixtures of $Si_3{}^{14}N_4$ and $Si_3{}^{15}N_4$ as the N source. $Si_3{}^{14}N_4$ was synthetized by Si nitridation using flowing N_2 in a Nabertherm 1-atm furnace, whereas isotopically enriched $Si_3{}^{15}N_4$ (~95% ^{15}N) was prepared as described by Leonova et al. (36). Mixtures of $Si_3{}^{14}N_4$ and $Si_3{}^{15}N_4$ were used to obtain variable initial $^{15}N/^{14}N$ ratios (between 0.1 and 8; Table 1) in the starting materials to assess the effect of ^{15}N spiking. Experimental procedures are described in *SI Appendix*, section S1.

Silicate- and Metal-Phase Nitrogen Analyses

Previous studies of N partitioning between metal and silicate phases (15, 17–22, 38) presented N abundance data obtained by electron probe microanalysis (EPMA). This in situ analytical method allows measuring N contents in metal alloys and silicate glasses in a polished section of an experimental charge with a detection limit as low as 0.03 wt% (17, 39) but is not adapted to isotopic measurements. Noble gas mass spectrometry enables bulk N-isotopic analyses (16) but, in our case, can only provide phase-specific isotopic compositions if the silicate glass and metal blobs are physically separated and measured independently, a challenging task depending on the sample texture (*SI Appendix*, Fig. S1).

We thus developed a method for in situ measurement of the N concentrations and isotopic compositions of quenched silicate and metal alloy phases by secondary ion mass spectrometry (SIMS) using the CAMECA IMS 1280 HR2 and 1270 at the Centre de Recherches Pétrographiques et Géochimiques (Nancy, France). Following the analytical protocol of Füri et al. (40), nitrogen isotopes in silicate glasses were measured with the IMS 1280 HR2 by spot analyses of $^{14}N^{16}O^-$ and $^{15}N^{16}O^-$ secondary molecular ions at mass numbers 30 and 31, respectively, at a nominal mass resolution $m/\Delta m = 14{,}000$ using a Cs^+ primary ion beam with a current of ~10 nA. A suite of reference glasses with known ^{14}N contents (40, 41) was used to determine the nitrogen concentration of each sample based on the $^{14}N^{16}O^-$ count rate normalized by the $^{16}O_2{}^-$ signal (*SI Appendix*, section S1). The nitrogen and carbon abundances and $^{15}N/^{14}N$ and $^{13}C/^{12}C$ ratios of metal phases were measured on the IMS 1270 using a Cs^+ primary ion beam with a current of ~2.4 nA. The size of the primary beam was set to ~5 μm to analyze metal blobs 10 to 65 μm in diameter. Carbon concentrations were measured as $^{12}C_2{}^-$, whereas nitrogen isotopes were measured as $^{12}C^{14}N^-$ and $^{12}C^{15}N^-$ at mass numbers 26 and 27, respectively, with a mass resolution of 8,000. Nitrogen elemental abundances were determined using the $^{12}C^{14}N^-/^{12}C_2{}^-$ ratio (42, 43). Owing to the low Si solubility in metals at the studied pressure–temperature (P–T) and fO_2 conditions (17), $^{28}Si^-$ was analyzed to monitor for potential silicate contamination during analyses. In parallel to the SIMS measurements, the nitrogen contents and $^{15}N/^{14}N$ ratios of reference silicate glasses (40) and metal reference materials were determined independently by noble gas mass spectrometry (*SI Appendix*, section S1). The use of ^{15}N-spiked samples allowed us to determine the $^{15}N/^{14}N$ ratios in the silicate and metal phases with average analytical uncertainties of 0.1‰ and 5.5‰, respectively. However, this uncertainty reached 91‰ for metal alloys in sample HB01, likely due to its highly heterogeneous C distribution.

Raman spectroscopic analyses were performed to determine N speciation in silicate glasses and metal alloy blobs (*SI Appendix*, section S1).

Sample Description

Experimental run products were composed of graphite-saturated mafic glass, close to the melt composition expected during a magma ocean stage (35), coexisting with variable amounts of an iron carbide metallic phase (*SI Appendix*, section S1 and Fig. S1). Among the experiments run, 6 samples had metal blobs of sufficient diameter (>7 μm) to permit SIMS analysis (*SI Appendix*, Fig. S1 and Table 1): only the data from these samples are presented herein. Silicate melts quenched to form large glass pools that were well separated from metal domains. Both silicate glasses and Fe–C–N alloys were compositionally homogeneous at the scale of EPMA analyses (~2 μm for metals; *SI Appendix*, section S1 and Tables S1 and S2). Along with Fe, the Pt and Si concentrations in the metal phases of all samples were measured by EPMA, which revealed Si contents below the detection limit

Table 1. Redox conditions, N elemental and isotopic compositions of the samples, and calculated N elemental and isotopic fractionations

Sample	fO_2 (ΔIW)	$[N]_{silicate}$, ppm)	$[N]_{metal}$, ppm	$D_N^{metal\text{-}silicate}$	$^{15}N/^{14}N$ initial*	$\delta^{15}N_{norm}^{silicate}$, ‰	$\delta^{15}N_{norm}^{metal}$, ‰	$\alpha^{metal\text{-}silicate}$	$\Delta^{15}N^{metal\text{-}silicate}$, ‰	$[H_2O]_{silicate}$, wt%†
HB01	−3.13	186 ± 2	28 ± 3	0.2 ± 0.2	0.09 ± 0.01	72 ± 10	−171 ± 28	0.77 ± 0.09	−257 ± 22	0.20 ± 0.04
HB05	−0.45	235 ± 36	1,571 ± 1,287‡	7 ± 2	0.67 ± 0.07	23 ± 3	−27 ± 4	0.95 ± 0.02	−49 ± 1	0.267 ± 0.002
HB15	−1.40	420 ± 22	682 ± 267	1.6 ± 0.8	8.0 ± 0.8	25 ± 4	−88 ± 13	0.89 ± 0.05	−116 ± 6	0.13 ± 0.03
HB3	−1.46	448 ± 5	1,493 ± 149	3.3 ± 0.2	0.80 ± 0.08	36 ± 5	−95 ± 13	0.87 ± 0.01	−135 ± 1	0.13 ± 0.09
HB4	−1.21	493 ± 12	1,488 ± 14	3.02 ± 0.05	0.85 ± 0.08	16 ± 2	−70 ± 10	0.92 ± 0.01	−89 ± 1	0.13 ± 0.03
A05	−2.15	855 ± 18	669 ± 126	0.8 ± 0.4	0.67 ± 0.07	11 ± 2	−14 ± 2	0.976 ± 0.002	−25 ± 1	0.19 ± 0.01

Reported errors are 2σ SDs.

*Estimated from the addition of $^{14}Si_3N_4$ and $^{15}Si_3N_4$ to the starting material. SDs on $\delta^{15}N_{norm}$ were estimated from weighing uncertainties related to the addition of Si_3N_4 to the starting material, and thus are larger than $\alpha^{metal\text{-}silicate}$ and $\Delta^{15}N^{metal\text{-}silicate}$ (‰), which were directly determined from SIMS measurements.

†Analyzed by SIMS (1280 HR2) following the method of Sobolev et al. (37). Details of the measurement conditions and standards are given in *SI Appendix*, section S1.

‡Large error due to C heterogeneities, likely graphite microinclusions, in the metal blobs.

and low amounts of Pt (<0.7 wt%). The major element compositions of silicate glasses and metal alloys determined by EPMA are presented in *SI Appendix*, Tables S1 and S2, respectively.

Table 1 presents sample oxygen fugacities, expressed as $\log f_{O2}$ (ΔIW), as estimated from the equilibrium reaction:

$$FeO_{silicate\ melt} = Fe_{liquid\ metal} + 1/2O_2. \quad [2]$$

Following this equilibrium, the fO_2 of each sample was calculated according to the method described in Dalou et al. (17), i.e., using the relationship between the mole fractions of FeO in the silicate melt (X_{FeO}^{melt}) and Fe in the liquid metal (X_{Fe}^{alloy}), the associated activity coefficients (γ_{FeO}^{melt} and γ_{Fe}^{alloy}, respectively), and the equilibrium constant, K, of the reaction (44):

$$\log_{10} fO_2 = \frac{2}{\ln(10)} \cdot \left[\ln\left(\frac{X_{FeO}^{melt}}{X_{Fe}^{alloy}}\right) - \ln\left(\gamma_{Fe}^{alloy}\right) + \ln\left(\gamma_{FeO}^{melt}\right) - \ln K \right]. \quad [3]$$

As described by Dalou et al. (17) and Grewal et al. (21, 22), we accounted for the effect of N and C on γ_{Fe}^{alloy} by extending the Wagner ε formalism (45) for nonideal interactions in liquid Fe alloys (46) via the MetalAct metal activity calculator (47), and we assumed $\gamma_{FeO}^{melt} = 1.2$ (48). Moreover, to permit direct comparison with the IW buffer, which is referenced to solid Fe metal, the activity coefficient of Fe was adjusted following the method of Stanley et al. (49). Finally, the resulting fO_2 was compared with the IW buffer as determined by Zhang et al. (50). This calculation was applied to our samples and all literature data presented for comparison in the figures. The fO_2 of our samples spanned from ΔIW −0.45 to −3.13.

We noted a significant loss of N (up to 75%) between the N added to the starting material and the total N measured in our experimental products. Speelmanns et al. (19, 20) observed a similar N loss during their experiments and suggested that N was lost to the graphite capsules enclosing their samples. Nonetheless, no significant difference in N loss is observed in N-partitioning experiments using single graphite (this study) or double platinum–graphite capsules (22). The samples showed no signs of vapor bubbles in the silicate glasses or metal alloy blobs. Although we cannot rule out the possible presence of submicroscopic bubbles in these phases, we assume that our experiments were N-vapor saturated and that N was lost to pores in the graphite capsules during the experiments. Therefore, the measured elemental and isotopic N fractionations between the metal and silicate phases occurred in an open system. The effect of N loss on N-isotopic fractionation is discussed in the following section.

The reported N and C contents and N-isotopic ratios and their associated SDs (2σ) were averaged from 2 to 6 analyses per sample (*SI Appendix*, Tables S2 and S3). Nitrogen and carbon contents in metal alloys are homogeneous within most samples, with SDs below 22% and 2% (2σ), respectively. The N contents of silicate glasses in each sample were homogeneous with a SD below 9%. As observed by Dalou et al. (17) and Füri et al. (40), the glasses contained micrometer-sized graphite inclusions, causing highly variable C signals over the course of an analysis and between distinct areas. Given that silicate glass N contents and isotopic compositions were measured as $^{14}N^{16}O^-/^{16}O_2^-$ and $^{15}N^{16}O^-/^{14}N^{16}O^-$ instead of $^{12}C^{14}N^-/^{12}C_2^-$ and $^{12}C^{15}N^-/^{12}C^{14}N^-$, this variability does not affect our N-elemental and -isotopic analyses (40). In samples for which metal blobs were large enough to perform multiple measurements (up to 4 analyses in HB05 and HB3, and 6 in HB4), homogeneous N-isotopic ratios were observed across the metal blobs, with SDs below 2% (2σ; *SI Appendix*, Table S3). Nitrogen contents in silicate glasses and metal alloy blobs are presented in Table 1, and carbon contents in metal phases in *SI Appendix*, Table S2.

It is very difficult to ensure that isotopic equilibrium is attained during isotope fractionation experiments that do not allow application of the "3-isotope method" (51). At temperatures from 1,600 °C to 1,800 °C, Li et al. (16) performed a series of experiments with increasing equilibration times between 30 and 120 min to ensure that isotopic equilibrium was attained. To promote isotopic equilibrium at 1,400 °C, we extended the run periods of our experiments to 6 h. Moreover, the homogeneity of N contents and $^{15}N/^{14}N$ ratios of the metal blobs and silicate glasses (*SI Appendix*, Table S3) strongly suggests that both chemical and isotopic equilibria were attained during our experiments.

fO_2 Control on N Partitioning Between Metal and Silicate Phases

Nitrogen partition coefficients between the metal and silicate phases, $D_N^{metal\text{-}silicate}$, were calculated as $D_N^{metal\text{-}silicate} = C_N^{metal}/C_N^{silicate}$, where C_N^{metal} and $C_N^{silicate}$ are the average N contents (wt%) of the metal alloys and silicate glasses, respectively (Table 1). With decreasing fO_2 from ΔIW −0.45 to −3.13, $D_N^{metal\text{-}silicate}$ decreases from 7 ± 2 to 0.2 ± 0.2, consistent with previous experimentally determined partition coefficients (15–22, 52, 53) (Fig. 1). Despite highly variable experimental parameters between studies (melt composition, P, and T), which produce scatter in the data trend (22), fO_2 remains the key parameter controlling N partitioning between the metal and silicate phases

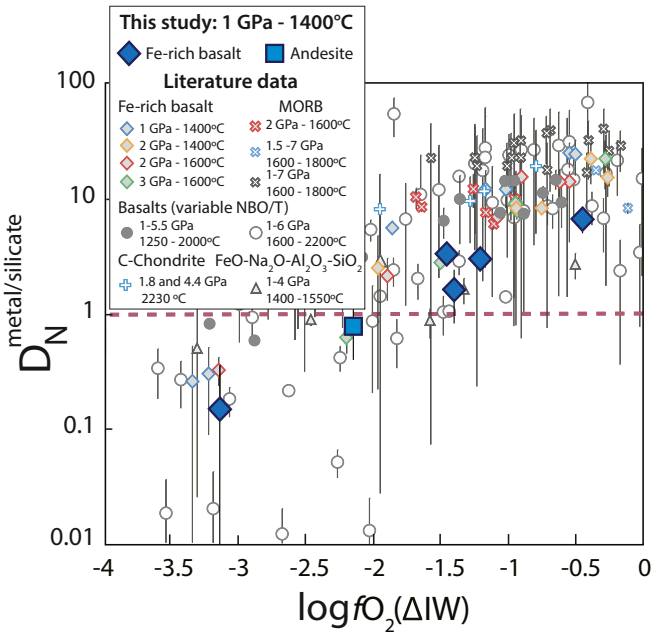

Fig. 1. $D_N^{metal\text{-}silicate}$ as a function of fO_2. Large symbols represent $D_N^{metal\text{-}silicate}$ values from this study, and small symbols are results from several previous studies: diamonds and red x's (17), blue x's (16), black x's (21), gray circles (20), empty circles (22), triangles (18, 37, 50, 51), and blue crosses (15). All fO_2 values were recalculated following the procedure described in the text. Following this calculation, only 2 of the 4 samples from Li et al. (16) have log $fO_2 <$ ΔIW. Error bars represent 2σ SDs. *P–T* conditions have only a small effect on $D_N^{metal\text{-}silicate}$ and explain the scatter among the overall decreasing trend with decreasing fO_2. Our data measured using SIMS (Fe-rich basalt and andesite) are in agreement with previously published $D_N^{metal\text{-}silicate}$ values measured by EPMA.

(17). $D_N^{metal\text{-}silicate}$ decreases with decreasing fO_2 due to the stabilization of N species in more reduced silicate melts (17).

In glasses, Raman spectroscopic analysis revealed that nitrogen is dissolved as N_2 and NH complexes (Fig. 2 *A* and *B*). At near-constant water content (Table 1), the ratio of NH to OH complexes (NH/OH, as determined from the Raman peak areas) increases with decreasing fO_2 (54), reflecting the increased N solubility in silicate glasses at more reducing conditions (17, 53). We note that vibrations associated with NH complexes are more intense in the Raman spectra of Fe-rich basalt samples (noted HB) than in the andesite A05 (Fig. 2*B*). Increased melt polymerization is known to increase N solubility and decrease the proportion of NH relative to N_2, i.e., the NH/N_2 ratio (29, 55). Therefore, the melt structure of sample A05 (more polymerized than the Fe-rich basalt glasses) favors N dissolution in the form of N_2 rather than NH complexes (Fig. 2 *A* and *B*). Overall, decreasing fO_2 has 2 effects: it increases both melt polymerization (due to increasing metal precipitation; *SI Appendix*, section S2) and the NH/N_2 ratio. Among the HB samples, we observe that the change of fO_2 primarily controls the NH/N_2 ratio, whereas at constant fO_2, melt polymerization governs the NH/N_2 ratio in silicate glasses (29).

Under nominally anhydrous conditions, N is assumed to chemically dissolve as nitride ions (N^{3-}) in reduced melts (below ΔIW −1.3) at 1 atm (56). The vibration mode of Si–N (near 800 cm^{-1}, ref. 57) is in the range of the dominant Si–O vibrations in silicate glasses. We therefore cannot ascertain the presence or absence of nitride species in our glasses by Raman spectroscopy.

Metal-Silicate N Isotopic Fractionation ($\Delta^{15}N^{metal\text{-}silicate}$)

The N-isotopic compositions of metal alloys ($^{15}N/^{14}N^{metal}$) and silicate glasses ($^{15}N/^{14}N^{silicate}$) in the Fe-rich basalts and haplo-andesite were determined via SIMS. The N-isotopic ratios, $^{15}N/^{14}N^{p}$, where p denotes the phase, were normalized to the initial N-isotopic composition of the starting material, $^{15}N/^{14}N^{initial}$, which ranged from 0.09 ± 0.01 to 8.0 ± 0.1 (Table 1). The normalized isotopic compositions are represented as follows:

$$\delta^{15}N^{p}_{norm}[‰] = 1{,}000 \cdot \left[\left(\frac{^{15}N/^{14}N^{p}}{^{15}N/^{14}N^{initial}}\right) - 1\right]. \quad [4]$$

Although these normalized values were not calculated relative to the atmospheric N-isotopic composition and are not directly comparable to $\delta^{15}N$ values measured in natural samples (40), they represent the magnitude of the observed change in the isotopic composition of each phase during the experiments. Fig. 3*A* reveals that N loss (in the form of N_2, NH_3, or both) by Rayleigh distillation during the experiments could increase the $\delta^{15}N^{silicate}$ values of the melt and may explain the positive $\delta^{15}N^{silicate}_{norm}$ values measured in the silicate glasses (Fig. 3*B*). In contrast, $\delta^{15}N^{metal}_{norm}$ is clearly negative compared with the initial $\delta^{15}N$ value (i.e., $\delta^{15}N_{norm} = 0‰$), suggesting that the metal phase becomes

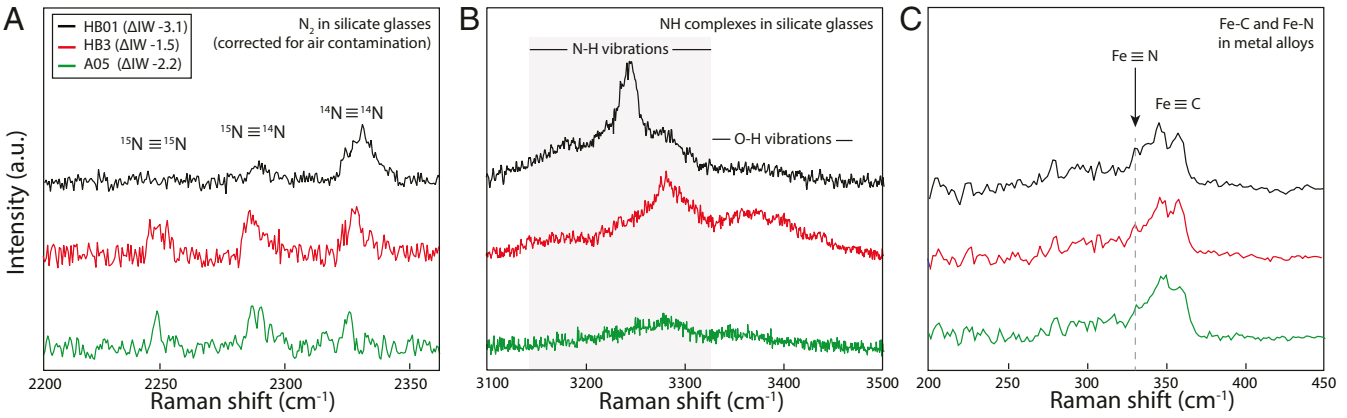

Fig. 2. Representative normalized Raman spectra of N species in silicate glasses and metal alloys of samples HB01, HB3, and A05: (*A*) N_2 isotopomers in silicate glasses, (*B*) NH complexes in silicate glasses, and (*C*) Fe–N bonds in metal alloys. The Raman shifts of N species are significantly different depending on speciation (N_2 versus NH complexes) and whether N is dissolved in metal alloy or silicate glass. Details of our Raman analysis are presented in *SI Appendix*, section S1.

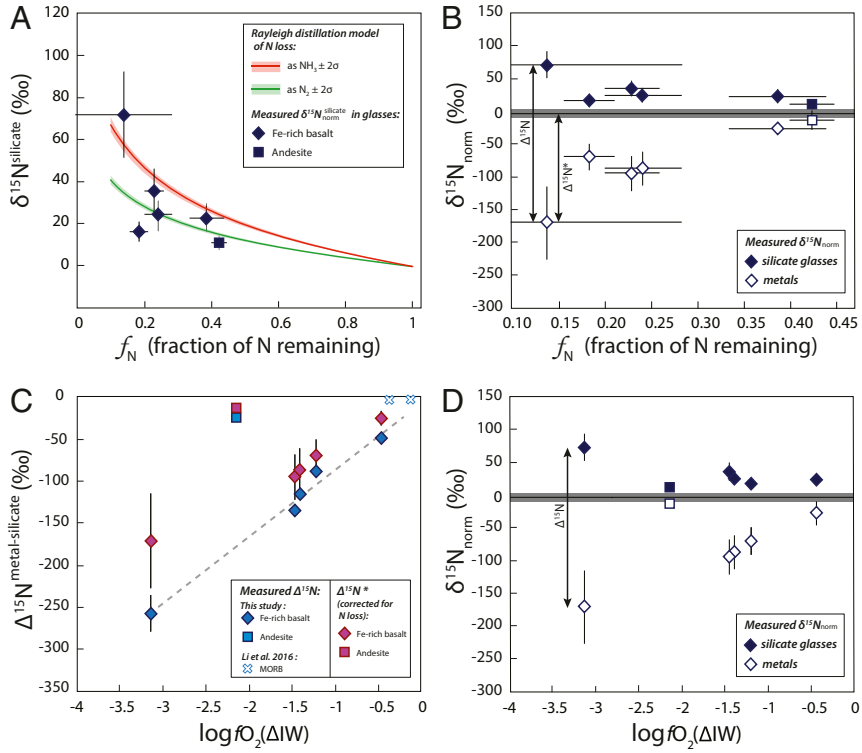

Fig. 3. Effect of N loss (*A* and *B*) and fO_2 (*C* and *D*) on N-isotopic fractionation $\Delta^{15}N^{metal\text{-}silicate}$. (*A*) Modeled effect of N loss by Rayleigh distillation on the $\delta^{15}N_{norm}$ values of silicate glasses as a function of f_N, the fraction of N remaining in the sample at the end of the experiments compared with the initial N content of the starting materials. The $\delta^{15}N^{silicate}_{norm}$ values represent measured $^{15}N/^{14}N^{silicate}$ ratios normalized to the initial $^{15}N/^{14}N$ ratio of the starting material (see text and Table 1). Rayleigh distillation was modeled for N_2 loss (green curve) and NH_3 loss (red curve) as $\delta^{15}N^{silicate} = 1{,}000 \cdot (f_N^{((1/\alpha)-1)} - 1)$, where α is the fractionation factor approximated here by $\sqrt{[m(^{15}N) + m(^{14}N)]/m(^{14}N_2)} = 1.02$ for N_2 loss and by $\sqrt{[m(^{15}N) + 3 \cdot m(H)]/[m(^{14}N) + 3 \cdot m(H)]} = 1.03$ for NH_3 loss. The positive $\delta^{15}N$ values measured in our silicate glasses can be explained by the Rayleigh distillation model, suggesting that N loss may have increased the $\delta^{15}N$ values of the silicate glasses. (*B*) Evolution of $\delta^{15}N$ in the silicate glasses (closed symbols) and in the metal blobs (open symbols) as a function of f_N. The $\delta^{15}N_{norm}$ values represent measured $^{15}N/^{14}N^{p}$ ratios (p representing the metallic or silicate phase) normalized to the initial $^{15}N/^{14}N$ ratio of the starting material (see text and Table 1), and the gray line at 0‰ represents the initial $\delta^{15}N_{norm}$ value. The difference between the $\delta^{15}N$ values measured in the metal and the silicate phases ($\delta^{15}N^{metal} - \delta^{15}N^{silicate}$) approximates the calculated $\Delta^{15}N^{metal\text{-}silicate}$ values. Considering that positive $\delta^{15}N^{silicate}_{norm}$ values may have been produced by N loss, the difference between the initial $\delta^{15}N_{norm}$ (0‰) and the $\delta^{15}N^{metal}_{norm}$ values corresponds to $\Delta^{15}N^*$, the N-isotopic fractionation corrected for N loss. (*C*) $\Delta^{15}N^{metal\text{-}silicate}$ as a function of fO_2, showing both calculated $\Delta^{15}N^{metal\text{-}silicate}$ (blue symbols) and $\Delta^{15}N^*$ (purple symbols). The small blue x's are reproduced from Li et al. (16), with fO_2 values recalculated following the procedure described in the text. Error bars represent 2σ SDs. Whereas the uncertainties on $\Delta^{15}N^{metal\text{-}silicate}$ are determined from the SDs on $^{15}N/^{14}N$ ratios measured by SIMS, the larger uncertainties on f_N, $\delta^{15}N_{norm}$ values, and $\Delta^{15}N^*$ are derived from the weighing uncertainties associated with the addition of $Si_3{}^{14}N_4$ and $Si_3{}^{15}N_4$ to the starting materials. The dashed line represents a linear regression ($r^2 > 0.9$) on the $\Delta^{15}N^{metal\text{-}silicate}$ values measured in Fe-rich basalt. $\Delta^{15}N^{metal\text{-}silicate}$ data describe 2 trends that can be explained by compositionally dependent differences in N speciation in the silicate glasses (see text). (*D*) Evolution of $\delta^{15}N_{norm}$ in the silicate glasses and metal blobs as a function of fO_2. This plot shows that positive $\delta^{15}N^{silicate}_{norm}$ values can also be produced by N-isotopic fractionation during metal segregation from the melt via the formation of ^{14}N–Fe bonds in the metal from ^{14}N in NH complexes in the melt. This process becomes more important as the fO_2 decreases due to the increasing stabilization of NH complexes in the melt under more reducing conditions.

enriched in ^{14}N during its segregation (Fig. 3*B*). Therefore, the observed positive $\delta^{15}N^{silicate}_{norm}$ values may result from N loss from the experiments and/or ^{14}N depletion during N partitioning into the metal phase.

The N-isotopic fractionations between metal and silicate in the samples (Table 1 and Fig. 3*C*) were calculated from the $^{15}N/^{14}N^{metal}$ and $^{15}N/^{14}N^{silicate}$ ratios measured by ion probe as follows:

$$\Delta^{15}N^{metal-silicate} \approx 1{,}000 \cdot \ln\left(\frac{^{15}N/^{14}N^{metal}}{^{15}N/^{14}N^{silicate}}\right). \quad [5]$$

They decrease from −49 ± 1‰ to −257 ± 22‰ with decreasing fO_2 from ΔIW −0.45 to −3.13. Such negative N-isotopic fractionations are in accord with equilibrium fractionation, during which the lightest isotopes favor bonds in the most reduced phase (23, 56), here as Fe–N (Fig. 2*C*). As the metal segregates from the silicate melt at isotopic equilibrium, it more favorably forms ^{14}N–Fe bonds than ^{15}N–Fe bonds, thereby depleting the silicate melt in ^{14}N; this process may increase the $\delta^{15}N^{silicate}_{norm}$ values. Alternatively, assuming that Rayleigh distillation alone produced the positive $\delta^{15}N^{silicate}_{norm}$ values observed in Fig. 3 *A* and *B*, then, when corrected for this process, $\delta^{15}N^{silicate}_{norm}$ can be assumed to remain at 0‰ during N partitioning into the metal phase. In this scenario, N-isotopic fractionations corrected for N loss, expressed as $\Delta^{15}N^* = \delta^{15}N^{metal}_{norm} - \delta^{15}N^{silicate}_{norm}$ with $\delta^{15}N^{silicate}_{norm}$ corrected to 0‰ (Fig. 3*B*), decrease from −27 ± 4‰ to −171 ± 28‰ with decreasing fO_2 from ΔIW −0.45 to −3.13 (Fig. 3*C*). Following this reasoning, $\Delta^{15}N^{metal\text{-}silicate}$ and $\Delta^{15}N^*$ represent the maximum and minimum bounds on metal–silicate N-isotopic fractionation in our experiments, respectively.

The $\Delta^{15}N^{metal\text{-}silicate}$ and $\Delta^{15}N^*$ values from this study are significantly lower than those obtained by Li et al. [$\Delta^{15}N^{metal\text{-}silicate}$ between 1.1 ± 2.8‰ and −5.5 ± 2.3‰ (16)]. This difference may be explained by the different *P*–*T* conditions of the 2 studies, although the results of Li et al. (16) show no pressure or temperature dependence over 1.5 to 7 GPa and 1,600 to 1,800 °C. It is,

however, questionable that they do not observe any temperature effect on $\Delta^{15}N^{metal\text{-}silicate}$ since, by definition, fractionation factors are inversely proportional to temperature (e.g., refs. 23 and 58). In addition, our large N-isotopic fractionations cannot be explained by ^{15}N spiking of our samples. As has been shown for H isotopic fractionation (59), $\Delta^{15}N^{metal\text{-}silicate}$ values are not dependent on the initial $^{15}N/^{14}N$ ratios of the experiments (Table 1). Instead, fO_2 is the key parameter differing between the 2 studies. The fO_2 of the samples of Li et al. (16) were between ΔIW −0.11 and −0.35, whereas the fO_2 of our samples varies from ΔIW −0.45 to −3.13. This observation implies an effect of fO_2 on $\Delta^{15}N^{metal\text{-}silicate}$.

These large N-isotopic fractionation values are comparable to estimates of H metal–silicate isotopic fractionation [between −55 and −285‰, modeled based on chondritic and mantle-like D/H values and H solubility in metal and silicate phases (60)], although, to our knowledge, no experimental data on metal–silicate fractionation are available for hydrogen or carbon isotopes. There are, however, experimental data available on H- and C-isotopic fractionations during other high-temperature magmatic processes. For instance, hydration or dehydration of silicate melts and nominally anhydrous minerals produces δD variations of up to 550‰ at 1,000 °C (61). During aqueous fluid–silicate melt interaction, H- and C-isotopic fractionations can reach 150‰ at 750 °C (56, 62–64). Among other isotope tracers of core formation, i.e., isotopes of heavier siderophile elements such as Si, Fe, Mo, Cr, Cu, and Ni (65), sulfur is the most comparable to N in terms of mass, solubility in reduced melts (66), and volatile behavior. However, experimentally determined metal–silicate S isotopic fractionation factors, $\Delta^{34}S^{metal\text{-}silicate}$, are only on the order of 0.1 to 1.2‰ between ΔIW −0.6 and −4.1 (67). Although the mass difference between N isotopes is 2.5 times larger than that between S isotopes, this difference is insufficient to explain the vast difference between the metal–silicate isotopic fractionations of N and S.

The Effects of fO_2 and N Speciation on $\Delta^{15}N^{metal\text{-}silicate}$

Following Bigeleisen and Mayer (30) and Urey (31), mass-dependent N-isotopic fractionation can be expressed as follows:

$$\Delta^{15}N^{metal-silicate} \propto 1{,}000 \cdot \left(\frac{\Delta m}{m_{14}m_{15}}\frac{\Delta F^{metal-silicate}}{T^2}\right), \quad [6]$$

where m_{14} and m_{15} are the atomic masses of ^{14}N and ^{15}N, respectively, Δm is their mass difference, $\Delta F^{metal-silicate}$ is the difference between the force constants acting on the isotopes in the metallic phase and the silicate melt ($\Delta F^{metal-silicate} = F_N^{metal} - F_N^{silicate}$, with F_N^{metal} and $F_N^{silicate}$ the effective force constants that depend on the chemical bond stiffness of N bonds in the metallic phase and silicate glass, respectively), and T is temperature in kelvin. In this study, at constant T, $\Delta F^{metal-silicate}$ is the only variable in the above equation acting on the N-isotopic fractionation between metal alloy and silicate melt, along with fO_2 variations. This parameter is related to vibrational frequency, ν_N, (30, 51), following:

$$\nu_N^p = \frac{1}{2\pi}\left(\frac{F_N^p}{\mu_N}\right)^{1/2}, \quad [7]$$

where ν_N was determined from the Raman vibration modes of N species in the metallic phases and the silicate glasses (Fig. 2) and μ_N is the reduced mass of the N-bearing molecule, calculated for N–H as $\mu(N\text{–}H) = [m_N \times m_H/(m_N + m_H)]$, with m_N and m_H being the atomic masses of N and H, respectively. More details on the principles and factors controlling stable isotopic fractionations can be found in Schauble (23) and Young et al. (51). Nitrogen dissolves in silicate glasses as molecular nitrogen (N_2) and NH complexes, and as Fe–N in metal alloys. N_2 has 3 isotopomers, $^{15}N\equiv^{15}N$, $^{15}N\equiv^{14}N$, and $^{14}N\equiv^{14}N$, with vibration modes in silicate glasses at 2,251, 2,287, and 2,326 cm^{-1}, respectively (Fig. 2*A*) (55), whereas the vibration mode of gaseous $^{14}N\equiv^{14}N$ is at 2,331 cm^{-1} (68). The vibration modes of NH complexes are between 3,180 and 3,350 cm^{-1} (Fig. 2*B*) (e.g., refs. 41 and 69). Fe–N vibrations in metal alloys are distinctly different, occurring at 338 cm^{-1} (Fig. 2*C*) (70). In comparison, S dissolves in metal alloys as Fe–S with vibration modes at 310 and 360 cm^{-1}, and in silicate melts as Fe–, Mg–, and Ca–S with vibration modes between 285 and 350 cm^{-1} (66). Although the vibration modes of complexes involving N or S have been determined for quenched silicate and metal, their equivalents in silicate melts and liquid metals at *HP–HT* are expected to vary only by a few cm^{-1}, as shown by Mysen (71) for the N_2 vibration mode in silicate melts and aqueous fluids. The observed vibration modes are directly related to the reduced masses μ_N and μ_S of the bonds formed by N and S, respectively, in the metal and silicate phases. As the relevant N bonds have very different reduced masses [μ(N–H) = 1 a.m.u., μ(N≡N) = 7 a.m.u., and μ(Fe–N) = 11 a.m.u.], the bonding of N with ions of very different masses directly produces large differences in the force constants (i.e., $\Delta F^{metal-silicate}$) acting on N isotopes in the 2 phases. In comparison, the smaller $\Delta F^{metal-silicate}$ values for S isotopes should result from the similar reduced masses of S bonds [μ(Mg–S) = 14 a.m.u., μ(Ca–S) = 18 a.m.u., and μ(Fe–S) = 20 a.m.u.]. Therefore, we conclude that the observed large N-isotopic fractionations relative to those of S are a consequence of the distinct N speciation between the metallic phase and the silicate melt.

The difference in vibrational frequencies and reduced masses between the metal and silicate phases is higher when N is dissolved as N–H complexes (e.g., NH_3) than as molecular N_2. The basic equation for equilibrium isotopic fractionation for stable isotopes, derived from Bigeleisen and Mayer (30), Urey (31), and Young et al. (51), can be expressed as follows:

$$\Delta^{15}N^{metal-silicate} = \frac{1{,}000}{24}\cdot\left(\frac{h}{k_bT}\right)^2\left(\frac{\Delta m}{m_{14}m_{15}}\right) \times\left[\left(\nu_N^{metal^2} - \nu_N^{silicate^2}\right)\left(\mu_N^{metal} - \mu_N^{silicate}\right)\right], \quad [8]$$

where h is Planck's constant (in joules per kelvin), k_b is the Boltzmann constant (in joules per hertz), T is temperature in kelvin, and ν_N^{metal} and $\nu_N^{silicate}$ denote the Raman vibration modes (in hertz) for the metal and silicate phases, respectively. From Eq. **8**, we estimate $\Delta^{15}N^{metal-silicate}$ to be −4 to −24‰ for N dissolved as N_2 or NH_3 in the silicate glass, respectively. Eq. **8** only considers N speciation differences between phases and assumes the absence of N interactions between molecular groups within each metal or silicate phase (e.g., different structural units). In general, however, this assumption is not valid for silicate melts because strong intermolecular bonds influence isotopic exchanges, thereby leading to a significant underestimation of the isotopic fractionation between distinct phases (e.g., refs. 59, 67, 72, and 73). However, this calculation shows that larger N-isotopic fractionations between the metal and silicate phases are produced depending on whether N is dissolved as N–H complexes or as molecular N_2. Accordingly, we can assume that higher NH/N_2 ratios in the melt produce larger metal–silicate N-isotopic fractionations than when N is present in the melt mainly as N_2. The increasing stabilization of NH complexes with decreasing fO_2 (Fig. 2*B*) therefore increases the observed metal–silicate N-isotopic fractionation among HB samples (Fig. 3*C* and *SI Appendix*, Fig. S5). In contrast, the $\Delta^{15}N^{metal\text{-}silicate}$ value of A05, −25 ± 1‰, is significantly smaller than those of the Fe-rich

basalts at equal fO_2 values (Fig. 3). This discrepancy may be explained by the lower NH/N_2 ratio of the andesite compared with that of the Fe-rich basalts.

Although not observed in our glasses, N dissolution as nitrides in the silicate melt would lead to smaller metal–silicate N-isotopic fractionation than for N dissolved as N_2 or N–H complexes, given the small difference in vibration modes between Fe–N in metals and Si–N in silicates ($\nu_N^{metal} - \nu_N^{silicate} = 462\ cm^{-1}$).

Nitrogen Isotopic Fractionation during Core Formation

N partitioning data (this study; refs. 15–22, 38, 52, and 53) show that, during terrestrial core–mantle differentiation, a fraction of N must have been removed from the magma ocean into the core-forming metals (Fig. 1). This N segregation produced an isotopic fractionation that depleted the metallic phase and enriched the silicate mantle in ^{15}N and was fundamentally dependent on the fO_2 conditions of the proto-mantle. Recent models (24, 28, 74) propose that the Earth accreted from small and highly reduced materials (ΔIW −5) during the first stages of its formation (60 to 70% of its mass), then from larger and more oxidized bodies (ΔIW −2) toward the end of accretion. Thus, the studied fO_2 range (ΔIW −3.1 to −0.5) represents plausible conditions of metal–silicate equilibration during the later stages of accretion and core formation (24, 74). During progressive oxidation from ΔIW −3.1 to −0.5, while the fraction of Earth's N increased in core-forming materials, the N-isotopic fractionation between the segregating metal and the silicate mantle would likely have decreased. These concurrent processes can be modeled using an equilibrium model of Earth's core–mantle differentiation (16). We adapted an equilibrium model of core formation that assumes complete equilibrium between the silicate mantle and the forming core (16) to account for progressive metal–silicate equilibration. This progressive equilibration is represented by the ratio of the masses of the silicate mantle and the bulk Earth (BE), m^{mantle}/m^{BE}, which varied between 1 (precore) and 0.67 (present-day Earth). The total mass M_N of N in the silicate mantle or BE is calculated from the following:

$$M_N^{mantle,\ BE} = C_N^{mantle,\ BE} \cdot m^{mantle,\ BE}, \quad [9]$$

where $C_N^{mantle,\ BE}$ is the N concentration in the mantle or BE, with

$$C_N^{mantle} = C_N^{BE} \cdot \left[\left(m^{mantle}/m^{BE} \right)^{\left(D_N^{metal-silicate} - 1 \right)} \right]. \quad [10]$$

The evolution of the N-isotopic composition of the mantle $\delta^{15}N_{mantle}$ during core formation is expressed as follows:

$$\delta^{15}N_{mantle} = \delta^{15}N_{BE} - \Delta^{15}N^{metal-silicate} \cdot \left(1 - \frac{M_N^{mantle}}{M_N^{BE}} \right). \quad [11]$$

This model is primarily dependent on the N-isotopic composition of the BE, $\delta^{15}N_{BE}$, and, to a lesser extent, C_N^{BE}, necessitating assumptions regarding the nature of the accreting bodies that formed the Earth. Considering an enstatite chondrite origin for Earth's N (11) and assuming no N was lost during accretion, the C_N^{BE} value of the proto-Earth was 160 ppm (75). For $\delta^{15}N_{BE}$, we chose to explore the 2 most extreme $\delta^{15}N$ values measured in enstatite chondrites: −45 and −15‰ (13). Over the fO_2 range ΔIW −3.1 to −0.5 (i.e., using the N partition coefficients and isotopic fractionation values derived from our experiments), a proto-Earth with a $\delta^{15}N_{BE}$ value of −45‰ would result in a $\delta^{15}N_{mantle}$ value between −25 and +1‰ at the end of core formation depending on the fO_2, whereas a $\delta^{15}N_{BE}$ value of −15‰ would result in a $\delta^{15}N_{mantle}$ value between +5 and +31‰ (Fig. 4). The modeled trend is linear at ΔIW −3 but logarithmic at IW, such that the difference between the 2 trends

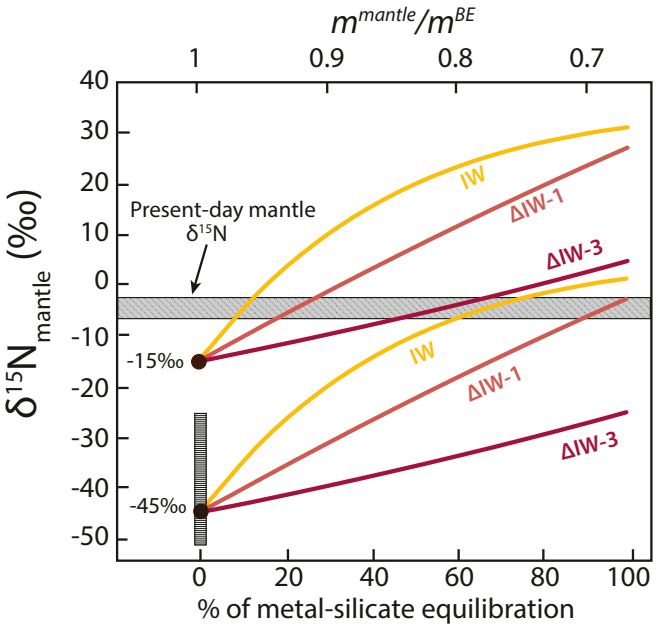

Fig. 4. Modeled $\delta^{15}N$ values of the silicate proto-mantle during core formation as a function of core–mantle equilibration and fO_2 conditions of the magma ocean. We explored 2 different $\delta^{15}N_{BE}$ values: the lowest (−45‰) and highest (−15‰) $\delta^{15}N$ values measured in enstatite chondrites (13). The respective values used for $D_N^{metal-silicate}$ and $\Delta^{15}N^{metal-silicate}$ were 7 and −49‰ at IW, 3.02 and −89‰ at ΔIW −1, and 0.2 and −257‰ at ΔIW −3.1 (Table 1). The present-day $\delta^{15}N$ value of the mantle is −5 ± 2‰ (gray bar; the thickness of the bar represents the 2σ SD), based on a compilation from diamonds and MORBs (3). This model assumes that $\Delta^{15}N^{metal-silicate}$ was not affected by Rayleigh distillation during the experiments, and thus only considers that the mantle's $\delta^{15}N$ value was modified by core–mantle fractionation without accounting for the effect of degassing. After 30% core–mantle (metal–silicate) equilibration, the modeled fO_2 variations account for a difference in the mantle $\delta^{15}N$ value of up to 27‰. The vertical bar between −51 and −25‰ represents the plausible range of $\delta^{15}N$ values of Earth's building blocks necessary to produce the present-day $\delta^{15}N_{mantle}$ value of −5 ± 2‰ at fO_2 conditions between ΔIW −3 and −0.5, assuming that core formation is the only process that fractionated N isotopes during the Earth's early history. At ΔIW −3.1, assuming a $\delta^{15}N_{BE}$ value of −25‰ for Earth's building blocks, complete metal–silicate equilibration is required to reach the present-day $\delta^{15}N_{mantle}$ value. In contrast, at IW, conditions under which N is siderophile, the present-day $\delta^{15}N_{mantle}$ value is attained at 60% metal–silicate equilibration from any source of N with a $\delta^{15}N_{BE} \geq -45‰$.

increases to a maximum of ∼27‰ at ∼60% metal–silicate equilibration, and then decreases to ∼20‰ at 100% metal–silicate equilibration (Fig. 4). This simple model demonstrates that the present-day mantle's $\delta^{15}N$ value of −5‰ could have been produced by core–mantle differentiation, assuming that enstatite chondrites are Earth's primary building blocks and the source of terrestrial N (or if $\delta^{15}N_{BE}$ was between −51 and −25‰; Fig. 4). Nevertheless, the outcome of this model is mainly controlled by the value of $\delta^{15}N_{BE}$ (Fig. 4) and therefore the source of Earth's N, which remains a matter of debate (5, 76).

On the Origin(s) and Evolution of Terrestrial N

Because the N-isotopic signatures of solar system objects and reservoirs are highly variable (77), N isotopes are key tracers of the source of terrestrial volatiles. Among chondrites, only enstatite chondrites have negative $\delta^{15}N$ values [−45 to −15‰ (13)]. This fact led Javoy et al. (5) to suggest that enstatite chondrites are the source of Earth's N. An enstatite chondrite-like $\delta^{15}N$ value of the proto-Earth is consistent with the scenario presented by Li et al. (16) and herein: N segregation into the core during proto-Earth differentiation could have increased the $\delta^{15}N$ value of the silicate

mantle from very negative values (as low as −45‰) to −5‰. In addition, the range of $\delta^{15}N$ values in Archean diamonds is similar to that of present-day diamonds and MORBs (11), suggesting that the mantle acquired its $\delta^{15}N$ value of −5‰ before the Archean (16). This would support the idea of a very negative proto-Earth $\delta^{15}N$ signature, similar to that of enstatite chondrites, and the subsequent enrichment of the mantle in ^{15}N by an early process, for instance core formation (16), possibly combined with magma ocean degassing and/or N recycling (7).

Nitrogen degassing (as N_2 or NH_3; Fig. 3*A*) from the magma ocean to the primitive atmosphere could also have increased the $\delta^{15}N_{mantle}$ value from an enstatite chondrite N-isotopic signature to the present-day value. Considering the highest reported $\delta^{15}N$ value for enstatite chondrites (−15‰), only 30% of magma ocean degassing is required to increase $\delta^{15}N_{mantle}$ by 10‰ to the present-day value of −5‰ assuming a Graham's law relationship (Fig. 3*A*). On the other hand, from an enstatite chondrite $\delta^{15}N$ value of −45‰, more than 75% of the initial N of the Earth needs to be degassed to increase $\delta^{15}N_{mantle}$ by 40‰ to the present-day value (Fig. 3*A*). Considering the low solubility of N_2 at low pressure under reduced conditions [<0.2 ppm at 1 atm between ΔIW −2 and IW (56)], large fractions of the proto-Earth's initial N content could have been degassed from a reduced magma ocean (e.g., refs. 20 and 35). However, these considerations are dependent on N solubility variations with fO_2 and fH_2 (which control the stabilization of NH complexes and thus N solubility) in mafic to ultramafic melts, for which data are sparse. In comparison, N recycling via subduction is insufficient to increase $\delta^{15}N_{mantle}$ by more than 5‰, even if subduction was initiated 4 Ga (78). As both magma ocean degassing and core formation may have increased the $\delta^{15}N$ value of the magma ocean, the source of terrestrial N might have had a N-isotopic signature significantly more negative than −45‰.

The very low $\delta^{15}N$ values of some Archean diamonds [−25 to −39‰, compared with −12 to +6‰ in most other Archean diamonds (12, 79)] have been suggested to represent relics of primordial N that have been preserved in an undegassed reservoir. The existence of such a primitive, undegassed mantle reservoir has been proposed to explain the low $^4He/^3He$ and $^{21}Ne/^{22}Ne$ [i.e., low $(U+Th)/^3He$ and $(U+Th)/^{22}Ne$] values of ocean island basalts (OIBs) [see review by Moreira (80)], as well as the preservation of a chondritic Xe component in the deep mantle (81). However, OIBs, typically associated with mantle plumes, exhibit high $\delta^{15}N$ values (around +2‰) akin to surficial N-isotopic compositions (7), suggesting that at least some of the N in OIBs is derived from recycled surficial N. The low $\delta^{15}N$ signature of the inferred undegassed reservoir responsible for Archean diamonds must have somehow been maintained during metal–silicate fractionation and core formation. The stable isotopic (i.e., $\delta^{13}C$) signature of diamonds can vary widely as a result of the redox state of the C–O–H–N fluids/melts from which they form (82, 83). Therefore, the extremely low $\delta^{15}N$ values of some Archean diamonds (12, 79) may similarly reflect fO_2 heterogeneities in the Archean mantle, although the effects of fO_2 on N speciation and isotopic fractionation in diamonds remain unknown (82).

Another possible origin of terrestrial N arises from the combined study of N isotopes and noble gases among solar system bodies. Based on the solar-like Ne isotopic composition of the mantle, Marty (76) discussed the possibility that the mantle has preserved some solar N. This scenario implies that precursor grains accreted during Earth's formation were first irradiated by the solar wind and preserved their solar volatile isotopic signature during Earth's accretion and differentiation [$\delta^{15}N_{IFSW} \leq$ −240‰; IFSW: implantation-fractionated solar wind (84, 85)]. Alternatively, a primordial solar atmosphere could have been captured by Earth's gravity and dissolved into the early magma ocean [$\delta^{15}N_{solar} = -383$‰ (e.g., ref. 86)]. Assuming a solar-like source of N for the proto-Earth, the mantle's N must have been significantly enriched in ^{15}N by N-isotopic fractionation during core–mantle differentiation, during magma ocean degassing (as N_2 and/or NH_3; Fig. 3*A*), and/or by the delivery of carbonaceous chondrites [$\delta^{15}N_{CC} = +15$ to +55‰ (14)] during late accretion and the addition of the late veneer.

Conclusions

We studied metal–silicate N-isotopic fractionation over a fO_2 range consistent with the inferred conditions of Earth's core formation. Our results reveal large N-isotopic fractionations over fO_2 conditions spanning 3 orders of magnitude. Such large fractionations can be explained by the vastly different N bonds formed in metal and silicate phases. The particularity of N, compared with other isotope tracers of core formation, is that it forms N_2 molecules or NH complexes in silicate melts, whereas it bonds as Fe–N in metal alloys. The strong dependence of N-isotopic fractionation on fO_2 conditions is a consequence of the increased solubility of NH complexes in silicate melts under increasingly reducing conditions. We also demonstrated that the NH/N_2 ratio and the N-isotopic fractionation depend on melt composition. Planetary magma oceans are expected to be mafic (close to our Fe-rich basalts) to ultramafic. Ultramafic melts (SiO_2-poor and MgO-rich) are difficult to quench from *HP–HT* to ambient conditions. Therefore, to advance our understanding of the effect of melt composition on N speciation and isotopic fractionation for extrapolation to such ultramafic melts at core-forming reduced conditions, experimental studies need to be performed using silicate melts spanning a large range of polymerization degrees.

Metal–silicate N partitioning coefficients increase significantly with increasing *P–T* conditions (22) because N solubility in metal blobs increases (15). How *P–T* conditions affect N_2 and NH solubility in silicate melts, and thereby metal–silicate N-isotopic fractionation, remains to be experimentally constrained over a wide range of *P–T* conditions. Although isotopic fractionations decrease with increasing temperature [$\Delta^{15}N \propto 1/T^2$ (20, 21)], an increase of pressure over tens of gigapascals should increase isotopic fractionations by increasing bond stiffness (51). However, how pressure affects bond stiffness in silicate glasses versus in metal alloys remains to be studied. At *P–T* conditions more representative of core–mantle equilibration in the terrestrial magma ocean [0 to 40 GPa and 2,000 to 3,000 K (87)], the magnitude of N-isotopic fractionation is expected to be smaller than determined in this study since the effect of *T* should dominate that of *P*. Thanks to our analytical developments, the N-content and -isotopic ratios of small phases (<15 μm in diameter) can now be measured in high-pressure (>10-GPa) experimental samples, which will allow the determination of N-isotopic fractionations at *P–T* conditions more representative of core–magma ocean equilibration conditions.

We have highlighted the fundamental effect of fO_2 on the evolution of the mantle's $\delta^{15}N$ value during core formation. We showed that fO_2 variations of 3 log units can produce a $\delta^{15}N$ variation of >20‰ in the silicate mantle after only 30% metal–silicate equilibration (Fig. 4). The magnitude of the N-isotopic fractionation observed here during metal–silicate segregation, larger fractionations under more reducing conditions, suggests that large N-isotopic fractionations could have also occurred during other high-temperature stages of Earth's formation, such as accretion and magma ocean crystallization and/or degassing.

ACKNOWLEDGMENTS. We thank Etienne Deloule, Nordine Bouden, and Laurent Zimmermann for their assistance and support during SIMS and noble gas mass spectrometry analyses. We also thank Mathieu Roskosz, Laurent Tissandier, Guillaume Paris, and Guillaume Caro for fruitful discussions, and Robert Dennen for English editing. We appreciate the insightful comments by 2 anonymous reviewers, which helped us to improve the

manuscript. This work was supported by the European Research Council under the European Union's Horizon 2020 research and innovation program (Grant Agreement 715028). M.L. was supported by the French Government Laboratory of Excellence Initiative ANR-10-LABX-0006 (ClerVolc Contribution 355). This is Centre de Recherches Pétrographiques et Géochimiques–CNRS Contribution 2713.

1. B. Johnson, C. Goldblatt, The nitrogen budget of Earth. *Earth Sci. Rev.* **148**, 150–173 (2015).
2. M. Javoy, F. Pineau, D. Demaiffe, Nitrogen and carbon isotopic composition in the diamonds of Mbuji Mayi (Zaire). *Earth Planet. Sci. Lett.* **68**, 399–412 (1984).
3. P. Cartigny, B. Marty, Nitrogen isotopes and mantle geodynamics: The emergence of life and the atmosphere–crust–mantle connection. *Elements* **9**, 359–366 (2013).
4. C. Thomazo, D. Papineau, Biogeochemical cycling of nitrogen on the early Earth. *Elements* **9**, 345–351 (2013).
5. M. Javoy, F. Pineau, H. Delorme, Carbon and nitrogen isotopes in the mantle. *Chem. Geol.* **57**, 41–62 (1986).
6. P. Cartigny, J. W. Harris, M. Javoy, Diamond genesis, mantle fractionations and mantle nitrogen content: A study of δ^{13}C–N concentrations in diamonds. *Earth Planet. Sci. Lett.* **185**, 85–98 (2001).
7. B. Marty, N. Dauphas, The nitrogen record of crust–mantle interaction and mantle convection from Archean to present. *Earth Planet. Sci. Lett.* **206**, 397–410 (2003).
8. V. Beaumont, F. Robert, Nitrogen isotope ratios of kerogens in Precambrian cherts: A record of the evolution of atmosphere chemistry? *Precambrian Res.* **96**, 63–82 (1999).
9. G. Paris *et al*., Nitrogen isotope record of a perturbed paleoecosystem in the aftermath of the end-Triassic crisis, Doniford section, SW England. *Geochem. Geophys. Geosyst.* **11**, Q08021 (2010).
10. P. Cartigny, M. Ader, A comment on "The nitrogen record of crust–mantle interaction and mantle convection from Archean to Present" by B. Marty and N. Dauphas [Earth Planet. Sci. Lett. 206 (2003) 397–410]. *Earth Planet. Sci. Lett.* **216**, 425–432 (2003).
11. M. Javoy, The birth of the Earth's atmosphere: The behaviour and fate of its major elements. *Chem. Geol.* **147**, 11–25 (1998).
12. M. Palot, P. Cartigny, J. W. Harris, F. V. Kaminsky, T. Stachel, Evidence for deep mantle convection and primordial heterogeneity from nitrogen and carbon stable isotopes in diamond. *Earth Planet. Sci. Lett.* **357**, 179–193 (2012).
13. M. M. Grady, I. P. Wright, L. P. Carr, C. T. Pillinger, Compositional differences in enstatite chondrites based on carbon and nitrogen stable isotope measurements. *Geochim. Cosmochim. Acta* **50**, 2799–2813 (1986).
14. J. F. Kerridge, Carbon, hydrogen and nitrogen in carbonaceous chondrites: Abundances and isotopic compositions in bulk samples. *Geochim. Cosmochim. Acta* **49**, 1707–1714 (1985).
15. M. Roskosz, M. A. Bouhifd, A. P. Jephcoat, B. Marty, B. O. Mysen, Nitrogen solubility in molten metal and silicate at high pressure and temperature. *Geochim. Cosmochim. Acta* **121**, 15–28 (2013).
16. Y. Li, B. Marty, S. Shcheka, L. Zimmermann, H. Keppler, Nitrogen isotope fractionation during terrestrial core-mantle separation. *Geochem. Perspect. Lett.* **2**, 138–147 (2016).
17. C. Dalou, M. M. Hirschmann, A. von der Handt, J. Mosenfelder, L. S. Armstrong, Nitrogen and carbon fractionation during core–mantle differentiation at shallow depth. *Earth Planet. Sci. Lett.* **458**, 141–151 (2017).
18. A. A. Kadik *et al*., Formation of N–C–O–H molecules and complexes in the basalt-basaltic andesite melts at 1.5 GPa and 1400°C in the presence of liquid iron alloys. *Geochem. Int.* **55**, 151–162 (2017).
19. I. M. Speelmanns, M. W. Schmidt, C. Liebske, Nitrogen solubility in core materials. *Geophys. Res. Lett.* **45**, 7434–7443 (2018).
20. I. M. Speelmanns, M. W. Schmidt, C. Liebske, The almost lithophile character of nitrogen during core formation. *Earth Planet. Sci. Lett.* **510**, 186–197 (2019).
21. D. S. Grewal, R. Dasgupta, C. Sun, K. Tsuno, G. Costin, Delivery of carbon, nitrogen, and sulfur to the silicate Earth by a giant impact. *Sci. Adv.* **5**, eaau3669 (2019).
22. D. S. Grewal *et al*., The fate of nitrogen during core-mantle separation on Earth. *Geochim. Cosmochim. Acta* **251**, 87–115 (2019).
23. E. A. Schauble, Applying stable isotope fractionation theory to new systems. *Rev. Mineral. Geochem.* **55**, 65–111 (2004).
24. D. C. Rubie *et al*., Heterogeneous accretion, composition and core–mantle differentiation of the Earth. *Earth Planet. Sci. Lett.* **301**, 31–42 (2011).
25. J. Badro, J. P. Brodholt, H. Piet, J. Siebert, F. J. Ryerson, Core formation and core composition from coupled geochemical and geophysical constraints. *Proc. Natl. Acad. Sci. U.S.A.* **112**, 12310–12314 (2015).
26. D. C. Rubie *et al*., Accretion and differentiation of the terrestrial planets with implications for the compositions of early-formed Solar System bodies and accretion of water. *Icarus* **248**, 89–108 (2015).
27. J. Wade, B. J. Wood, The oxidation state and mass of the Moon-forming impactor. *Earth Planet. Sci. Lett.* **442**, 186–193 (2016).
28. C. Cartier, T. Hammouda, M. Boyet, M. A. Bouhifd, J. L. Devidal, Redox control of the fractionation of niobium and tantalum during planetary accretion and core formation. *Nat. Geosci.* **7**, 573–576 (2014).
29. B. O. Mysen, M. L. Fogel, Nitrogen and hydrogen isotope compositions and solubility in silicate melts in equilibrium with reduced (N+H)-bearing fluids at high pressure and temperature: Effects of melt structure. *Am. Mineral.* **95**, 987–999 (2010).
30. J. Bigeleisen, M. G. Mayer, Calculation of equilibrium constants for isotopic exchange reactions. *J. Chem. Phys.* **15**, 261–267 (1947).
31. H. C. Urey, The thermodynamic properties of isotopic substances. *J. Chem. Soc.* **1947**, 562–581 (1947).
32. M. M. Hirschmann, Magma ocean influence on early atmosphere mass and composition. *Earth Planet. Sci. Lett.* **341**, 48–57 (2012).
33. L. S. Armstrong, M. M. Hirschmann, B. D. Stanley, E. G. Falksen, S. D. Jacobsen, Speciation and solubility of reduced C–O–H–N volatiles in mafic melt: Implications for volcanism, atmospheric evolution, and deep volatile cycles in the terrestrial planets. *Geochim. Cosmochim. Acta* **171**, 283–302 (2015).
34. H. L. Zhang, P. A. Solheid, R. A. Lange, A. von der Handt, M. M. Hirschmann, Accurate determination of $Fe^{3+}/\sum Fe$ of andesitic glass by Mössbauer spectroscopy. *Am. Mineral.* **100**, 1967–1977 (2015).
35. M. M. Hirschmann, Constraints on the early delivery and fractionation of Earth's major volatiles from C/H, C/N, and C/S ratios. *Am. Mineral.* **101**, 540–553 (2016).
36. E. Leonova, J. Grins, M. Shariatgorji, L. L. Ilag, M. Edén, Solid-state NMR investigations of Si-29 and N-15 enriched silicon nitride. *Solid State Nucl. Magn. Reson.* **36**, 11–18 (2009).
37. A. V. Sobolev *et al*., Komatiites reveal a hydrous Archaean deep-mantle reservoir. *Nature* **531**, 628–632 (2016).
38. A. A. Kadik *et al*., Solution behavior of reduced N–H–O volatiles in FeO–Na_2O–SiO_2–Al_2O_3 melt equilibrated with molten Fe alloy at high pressure and temperature. *Phys. Earth Planet. Inter.* **214**, 14–24 (2013).
39. A. von der Handt, C. Dalou, Quantitative EPMA of nitrogen in silicate glasses. *Microsc. Microanal.* **22** (suppl. 3), 1810–1811 (2016).
40. E. Füri, E. Deloule, C. Dalou, Nitrogen abundance and isotope analysis of silicate glasses by secondary ionization mass spectrometry. *Chem. Geol.* **493**, 327–337 (2018).
41. J. Mosenfelder *et al*., Nitrogen incorporation in silicates and metals: Results from SIMS, EPMA, FTIR, and laser-extraction mass spectrometry. *Am. Mineral.* **104**, 31–46 (2019).
42. N. Sugiura, Ion probe measurements of carbon and nitrogen in iron meteorites. *Meteorit. Planet. Sci.* **33**, 393–409 (1998).
43. N. Sugiura, S. Zashu, M. Weisberg, M. Prinz, A nitrogen isotope study of bencubbinites. *Meteorit. Planet. Sci.* **35**, 987–996 (2000).
44. E. Médard, C. A. McCammon, J. A. Barr, T. L. Grove, Oxygen fugacity, temperature reproducibility, and H_2O contents of nominally anhydrous piston-cylinder experiments using graphite capsules. *Am. Mineral.* **93**, 1838–1844 (2008).
45. C. Wagner, *Thermodynamics of Alloys* (Addison-Wesley, Reading, MA, 1962).
46. J. Wade, B. J. Wood, Core formation and the oxidation state of the Earth. *Earth Planet. Sci. Lett.* **236**, 78–95 (2005).
47. B. J. Wood, J. Wade, A. Norris, MetalAct Website (2017) http://norris.org.au/expet/metalact/. Accessed 19 February 2019.
48. H. S. C. O'Neill, S. M. Eggins, The effect of melt composition on trace element partitioning: An experimental investigation of the activity coefficients of FeO, NiO, CoO, MoO_2 and MoO_3 in silicate melts. *Chem. Geol.* **186**, 151–181 (2002).
49. B. D. Stanley, M. M. Hirschmann, A. C. Withers, Solubility of COH volatiles in graphite-saturated martian basalts. *Geochim. Cosmochim. Acta* **129**, 54–76 (2014).
50. H. L. Zhang, M. M. Hirschmann, E. Cottrell, M. Newville, A. Lanzirotti, Structural environment of iron and accurate determination of $Fe^{3+}/\Sigma Fe$ ratios in andesitic glasses by XANES and Mössbauer spectroscopy. *Chem. Geol.* **428**, 48–58 (2016).
51. E. D. Young *et al*., High-temperature equilibrium isotope fractionation of non-traditional stable isotopes: Experiments, theory, and applications. *Chem. Geol.* **395**, 176–195 (2015).
52. A. A. Kadik *et al*., Influence of oxygen fugacity on the solubility of nitrogen, carbon, and hydrogen in FeO–Na_2O–SiO_2–Al_2O_3 melts in equilibrium with metallic iron at 1.5 GPa and 1400 °C. *Geochem. Int.* **49**, 429–438 (2011).
53. A. A. Kadik *et al*., Solubility of nitrogen, carbon, and hydrogen in FeO–Na_2O–Al_2O_3–SiO_2 melt and liquid iron alloy: Influence of oxygen fugacity. *Geochem. Int.* **53**, 849–868 (2015).
54. C. Dalou, C. Le Losq, M. M. Hirschmann, S. D. Jacobsen, E. Füri, Evolution of COHN volatile species in the magma ocean during core formation. *AGU Fall Meeting Abstr.* V31E-01 (2017). http://adsabs.harvard.edu/abs/2017AGUFM.V31E..01D. Accessed 12 December 2018.
55. M. Roskosz, B. O. Mysen, G. D. Cody, Dual speciation of nitrogen in silicate melts at high pressure and temperature: An experimental study. *Geochim. Cosmochim. Acta* **70**, 2902–2918 (2006).
56. G. Libourel, B. Marty, F. Humbert, Nitrogen solubility in basaltic melt. Part I. Effect of oxygen fugacity. *Geochim. Cosmochim. Acta* **67**, 4123–4135 (2003).
57. E. Soignard, P. F. McMillan, Raman spectroscopy of γ-Si_3N_4 and γ-Ge_3N_4 nitride spinel phases formed at high pressure and high temperature: Evidence for defect formation in nitride spinels. *Chem. Mater.* **16**, 3533–3542 (2004).
58. C. Kendall, E. A. Caldwell, "Fundamentals of isotope geochemistry" in *Isotope Tracers in Catchment Hydrology*, C. Kendall, J. J. McDonnell, Eds. (Elsevier, Amsterdam, 1998), pp. 51–86.
59. C. Dalou, C. Le Losq, B. O. Mysen, In situ study of the fractionation of hydrogen isotopes between aluminosilicate melts and coexisting aqueous fluids at high pressure and high temperature–Implications for the δD in magmatic processes. *Earth Planet. Sci. Lett.* **426**, 158–166 (2015).
60. J. Wu *et al*., Origin of Earth's water: Chondritic inheritance plus nebular ingassing and storage of hydrogen in the core. *J. Geophys. Res. Planets* **123**, 2671–2712 (2018).
61. M. Roskosz *et al*., Kinetic D/H fractionation during hydration and dehydration of silicate glasses, melts and nominally anhydrous minerals. *Geochim. Cosmochim. Acta* **233**, 14–32 (2018).
62. B. O. Mysen, T. Tomita, E. Ohtani, A. Suzuki, Speciation of and D/H partitioning between fluids and melts in silicate-DOHCN systems determined *in-situ* at upper mantle temperatures, pressures, and redox conditions. *Am. Mineral.* **99**, 578–588 (2014).

63. B. Mysen, Experimentally-determined carbon isotope fractionation in and between methane-bearing melt and fluid to upper mantle temperatures and pressures. *Earth Planet. Sci. Lett.* **445**, 28–35 (2016).
64. B. Mysen, Experimental *in-situ* carbon solution mechanisms and isotope fractionation in and between (C–O–H)-saturated silicate melt and silicate-saturated (C–O–H) fluid to upper mantle temperatures and pressures. *Earth Planet. Sci. Lett.* **459**, 352–361 (2017).
65. B. Bourdon, M. Roskosz, R. C. Hin, Isotope tracers of core formation. *Earth Sci. Rev.* **181**, 61–81 (2018).
66. O. Namur, B. Charlier, F. Holtz, C. Cartier, C. McCammon, Sulfur solubility in reduced mafic silicate melts: Implications for the speciation and distribution of sulfur on Mercury. *Earth Planet. Sci. Lett.* **448**, 102–114 (2016).
67. J. Labidi *et al*., Experimentally determined sulfur isotope fractionation between metal and silicate and implications for planetary differentiation. *Geochim. Cosmochim. Acta* **175**, 181–194 (2016).
68. W. R. Fenner, H. A. Hyatt, J. M. Kellam, S. P. S. Porto, Raman cross section of some simple gases. *J. Opt. Soc. Am.* **63**, 73–77 (1973).
69. B. O. Mysen, S. Yamashita, N. Chertkova, Solubility and solution mechanisms of NOH volatiles in silicate melts at high pressure and temperature-amine groups and hydrogen fugacity. *Am. Mineral.* **93**, 1760–1770 (2008).
70. L. Lei, W. Yin, X. Jiang, S. Lin, D. He, Synthetic route to metal nitrides: High-pressure solid-state metathesis reaction. *Inorg. Chem.* **52**, 13356–13362 (2013).
71. B. Mysen, Silicate solution, cation properties, and mass transfer by aqueous fluid in the Earth's interior. *Prog. Earth Planet. Sci.* **5**, 1–18 (2018).
72. Y. Wang, S. X. Cody, D. Foustoukos, B. O. Mysen, G. D. Cody, Very large differences in intramolecular DH partitioning in hydrated silicate melts synthesized at upper mantle pressures and temperatures. *Am. Mineral.* **100**, 1182–1189 (2015).
73. C. Le Losq, B. O. Mysen, G. D. Cody, Intramolecular fractionation of hydrogen isotopes in silicate quenched melts. *Geochem. Perspect. Lett.* **2**, 87–94 (2016).
74. A. Morbidelli *et al*., Source regions and timescales for the delivery of water to the Earth. *Meteorit. Planet. Sci.* **35**, 1309–1320 (2000).
75. E. A. Bergin, G. A. Blake, F. Ciesla, M. M. Hirschmann, J. Li, Tracing the ingredients for a habitable earth from interstellar space through planet formation. *Proc. Natl. Acad. Sci. U.S.A.* **112**, 8965–8970 (2015).
76. B. Marty, The origins and concentrations of water, carbon, nitrogen and noble gases on Earth. *Earth Planet. Sci. Lett.* **313**, 56–66 (2012).
77. E. Füri, B. Marty, Nitrogen isotope variations in the Solar System. *Nat. Geosci.* **8**, 515–522 (2015).
78. A. Mallik, Y. Li, M. Wiedenbeck, Nitrogen evolution within the Earth's atmosphere–mantle system assessed by recycling in subduction zones. *Earth Planet. Sci. Lett.* **482**, 556–566 (2018).
79. P. Cartigny, S. Boyd, J. Harris, M. Javoy, Nitrogen isotopes in peridotitic diamonds from Fuxian, China: The mantle signature. *Terra. Nova* **9**, 175–179 (1997).
80. M. Moreira, Noble gas constraints on the origin and evolution of Earth's volatiles. *Geochem. Perspect.* **2**, 229–230 (2013).
81. A. Caracausi, G. Avice, P. G. Burnard, E. Füri, B. Marty, Chondritic xenon in the Earth's mantle. *Nature* **533**, 82–85 (2016).
82. P. Cartigny, M. Palot, E. Thomassot, J. W. Harris, Diamond formation: A stable isotope perspective. *Annu. Rev. Earth Planet Sci.* **42**, 699–732 (2014).
83. H. Bureau, L. Remusat, I. Esteve, D. L. Pinti, P. Cartigny The growth of lithospheric diamonds. *Sci. Adv.* **4**, eaat1602 (2018).
84. K. Hashizume, M. Chaussidon, B. Marty, F. Robert, Solar wind record on the moon: Deciphering presolar from planetary nitrogen. *Science* **290**, 1142–1145 (2000).
85. S. Péron, M. Moreira, A. Agranier, Origin of light noble gases (He, Ne, and Ar) on Earth: A review. *Geochem. Geophys. Geosyst.* **19**, 979–996 (2018).
86. B. Marty, M. Chaussidon, R. C. Wiens, A. J. G. Jurewicz, D. S. Burnett, A ^{15}N-poor isotopic composition for the solar system as shown by Genesis solar wind samples. *Science* **332**, 1533–1536 (2011).
87. D. Andrault *et al*., Solidus and liquidus profiles of chondritic mantle: Implication for melting of the Earth across its history. *Earth Planet Sci. Lett.* **304**, 251–259 (2011).